# Exploration of the Temperature Sensing Ability of La$_2$MgTiO$_6$:Er$^{3+}$ Double Perovskites Using Thermally Coupled and Uncoupled Energy Levels

**Thi Hong Quan Vu** [ID]**, Bartosz Bondzior, Dagmara Stefańska and Przemysław J. Dereń *** [ID]

Institute of Low Temperature and Structure Research, Polish Academy of Sciences, Okólna 2,
50-422 Wrocław, Poland; q.vu@intibs.pl (T.H.Q.V.); b.bondzior@intibs.pl (B.B.); d.stefanska@intibs.pl (D.S.)
***** Correspondence: p.deren@intibs.pl

**Abstract:** This work aimed to explore the temperature-sensing performance of La$_2$MgTiO$_6$:Er$^{3+}$ double perovskites based on thermally coupled and uncoupled energy levels. Furthermore, the crystal structure, chemical composition, and morphology of the samples were investigated by powder X-ray diffraction, energy-dispersive X-ray spectroscopy, and scanning electron microscopy, respectively. The most intense luminescence was observed for the sample doped with 5% Er$^{3+}$. The temperature-dependent emission spectra of La$_2$MgTiO$_6$:5% Er$^{3+}$ were investigated in the wide range of 77–398 K. The highest sensitivity of the sample was equal to 2.98%/K corresponding to the thermally coupled energy level $^2H_{11/2} \rightarrow {}^4I_{15/2}$ and $^4S_{3/2} \rightarrow {}^4I_{15/2}$ as compared to 1.9%/K, obtained for the uncoupled energy level $^2H_{11/2} \rightarrow {}^4I_{15/2}$ and $^2H_{9/2} \rightarrow {}^4I_{15/2}$. Furthermore, the 300 K luminescent decay profiles were analyzed using the Inokuti–Hirayama model. The energy transfer among Er$^{3+}$ ions was mainly regulated by the dipole–dipole mechanism. The critical transfer distance R$_0$, critical concentration C$_0$, energy transfer parameter C$_{da}$, and energy transfer probability W$_{da}$ were 9.81 Å, $2.53 \times 10^{20}$ ions·cm$^{-3}$, $5.38 \times 10^{-39}$ cm$^6$·s$^{-1}$, and 6020 s$^{-1}$, respectively.

**Keywords:** double perovskites; La$_2$MgTiO$_6$; erbium; luminescence; luminescent thermometry

## 1. Introduction

Double perovskite compounds (DP) are among the most intensely studied materials because of their interesting chemical and physical properties, as well as their diverse applications stemming from the compositional flexibility of their structure. La$_2$MgTiO$_6$ (LMT), a representative of the double perovskite family, has recently been extensively investigated as a host of many lanthanide ions [1–3]. The energy transfer process from TiO$_6$ groups to lanthanides ions takes place very efficiently [3]. Erbium ions have been widely applied in eye-safe lasers, optical communications, or lighting owing to their broad spectral range spans in the ultraviolet, visible, and near-infrared regions [4–6]. The most universal approach for LMT is a white-light conversion material related to emission from Sm$^{3+}$ and Eu$^{3+}$ [7], Mn$^{4+}$ and Yb$^{3+}$ [8], Bi$^{3+}$ [9], Eu$^{3+}$ [10], Eu$^{2+}$ [11], Mn$^{4+}$ [12–15], and Gd$^{3+}$, Bi$^{3+}$, Sm$^{3+}$, and Eu$^{3+}$ ions [16]. Furthermore, an ample potential for optical thermal sensing has recently been demonstrated through these studies including LMT:Pr$^{3+}$ [17], LMT:Eu$^{3+}$ [3], and LMT:Nd$^{3+}$ [2].

Temperature is one of the most important physical parameters which is present in many fields of science and life. In the last few decades, there has been an explosion of research on such optical thermometry [17–23] to fulfil the requirements of fast growth in a myriad of fields including chemistry, physics, biomedicine, and industry. Indeed, noncontact thermometers possess numerous advantages, such as remote, handy, and precise application, high spatial resolution, and a broad operating temperature range as compared to the conventional thermometers [24]. What is more, they can operate in harsh conditions, e.g., high pressure, corrosive, and very low or high temperature, where the

traditional techniques are infeasible [22]. To design luminescent thermometry, taking into account the reliance of peak position, emission intensity, and lifetime when elevating temperature, the sensitivity of thermometers should be estimated. The ratio of emission intensity between two distinct transitions is preferable since it is an external interference-independent factor [24]. It is worth noting that there has only been one investigation into LMT:$Er^{3+}$ published recently with regard to temperature readout application. However, it was synthesized using the conventional solid-state method, the working temperature range was quite narrow, and it was only focused on thermally coupled levels [25].

Therefore, a comprehensive investigation of the temperature-sensing ability of LMT:$Er^{3+}$ synthesized via the coprecipitation method was conducted by exploring both thermally coupled and uncoupled energy levels. The well-known thermally coupled levels correspond to the transitions $^2H_{11/2} \rightarrow {}^4I_{15/2}$ and $^4S_{3/2} \rightarrow {}^4I_{15/2}$, which are separated from each other by 592 $cm^{-1}$. The energy gap between these levels should be neither too close to overlap nor too far to be easily populated by the other; moreover, it should be in the range from 200 $cm^{-1}$ to 2000 $cm^{-1}$ [26]. Nonetheless, uncoupled levels, which are related to the phonon-assisted process, have also gained significant attention for temperature sensing [18,27,28]. This is due to the fact that the phonon-assisted process enhanced by elevating temperature is also related to absorption, emission, and energy transfer. Thus, the exploration of all possibilities including thermally coupled and uncoupled levels is crucial to choose the highest sensitivity with the lowest uncertainty.

The aim of this work was to explore the temperature sensing performance of a novel double perovskite LMT:$Er^{3+}$ as a function of the ratio of emission intensity of thermally coupled and uncoupled energy levels of $Er^{3+}$ ions. Additionally, the structural, morphological, and spectroscopic properties including absorption and emission spectra were investigated. The energy transfer mechanism among $Er^{3+}$ ions and the characteristics of luminescent decay kinetics were clarified using the Inokuti–Hirayama model.

## 2. Experimental

### 2.1. Synthesis

$La_2MgTiO_6$:x $Er^{3+}$ (where x = 0%, 0.1%, 0.5%, 1%, 3%, 5%, or 7%) was successfully obtained via the coprecipitation method. The procedure was calculated for 0.5 g of sample. The erbium ions were incorporated into the lanthanum site in the structure. All precursors used for the syntheses were purchased from the Alfa Aesar company (Kandel, Germany), including lanthanum acetate ($La(CH_3COO)_3 \cdot 1.5H_2O$, 99.9%), magnesium nitrate ($Mg(NO_3)_2 \cdot 6H_2O$, 99.97%), titanium isopropoxide ($Ti(C_3H_7O)_4$, 95%), erbium oxide ($Er_2O_3$, 99.99%), nitric acid ($HNO_3$, 65%, POCH), and ammonium hydroxide ($NH_4OH$, 25%, CHEMPUR). The synthesis method, annealing time, and sintering temperature were described in previous publications [2,3]. Firstly, the proper amounts of erbium oxide and titanium isopropoxide were separately diluted in nitric acid solution. Afterward, the prepared solution of titanium isopropoxide was added into the mixture of the aqueous solution containing lanthanum, magnesium, and erbium ions (for doped samples). However, it should be emphasized that a 10% excess amount of magnesium ions was applied due to the likelihood of the sublimation of magnesium ions during the high-temperature sintering process. To obtain the precipitate, a solution of ammonium hydroxide (1 mL) was added. The obtained precipitate was dried at 80 °C for 24 h on a heater. Then, it was sintered at 600 °C for 12 h in a porcelain crucible. The second annealing was conducted at 1300 °C for 8 h in a corundum crucible in air. Grinding for a few minutes was necessary after each step of annealing.

### 2.2. Characterization

The powder X-ray diffractions of all samples were measured on an X'Pert ProPANalytical (PANalytical, Almelo, The Netherlands) using an X-ray diffractometer with Cu $K_\alpha$ radiation ($\lambda$ = 1.54056 Å) in a 2θ range from 10° to 90° with a step size of Δ2θ = 0.02°. The morphology and chemical composition of LMT:5% $Er^{3+}$ were investigated using a scanning

electron microscope FEI NOVA NanoSEM230 (FEI, Hillsboro, OR, USA). To determine the absorption spectrum of LMT:7% $Er^{3+}$, a Varian Cary 5E UV/Vis–NIR spectrophotometer (Varian Incorporation, Palo Alto, CA, USA) was used. The 300 K emission spectra of all samples were obtained using a Hamamatsu Photonic multichannel analyzer PMA-12 (Hamamatsu Photonics K.K, Shizuoka, Japan) along with a BT-CCD linear image sensor. Furthermore, a McPherson spectrometer linear PIXcel detector (McPherson Incorporation, Chelmsford, MA, USA) equipped with an 808 diode laser was used for infrared emission measurement. The 300 K emission decay profiles were recorded with a Lecroy digital oscilloscope (Teledyne Technologies, New York, NY, USA) using an excitation source of Nd:YAG. The thermal quenching measurements were measured using the Hamamatsu Photonic multichannel analyzer PMA-12 equipped with the BT-CCD linear image sensor. The temperature of the samples was controlled by a Linkam THMS 600 Heating/Freezing Stage (The McCRONE Group, Westmont, IL, USA).

## 3. Results and Discussion

### 3.1. Structural and Morphological Characterization

The XRD patterns of all prepared samples and the standard pattern of $La_2MgTiO_6$ (ICSD no. 86852) are shown in Figure 1. All samples crystallized in an orthorhombic structure with space group *Pbnm* (62) with the following lattice parameters: a = 5.5609 (1), b = 5.5738 (1), c = 7.8623 (2), V = 243.69 Å$^3$, and Z = 4 [2,3]. No impurity traces were found. The main diffraction lines of the samples observed at 2θ values of 22.72°, 32.33°, 39.87°, 46.30°, 52.16°, 57.59°, 67.52°, and 76.82° were assigned to the lattice planes (hkl) of (110), (112), (202), (220), (310), (132), (400), and (116), respectively [29].
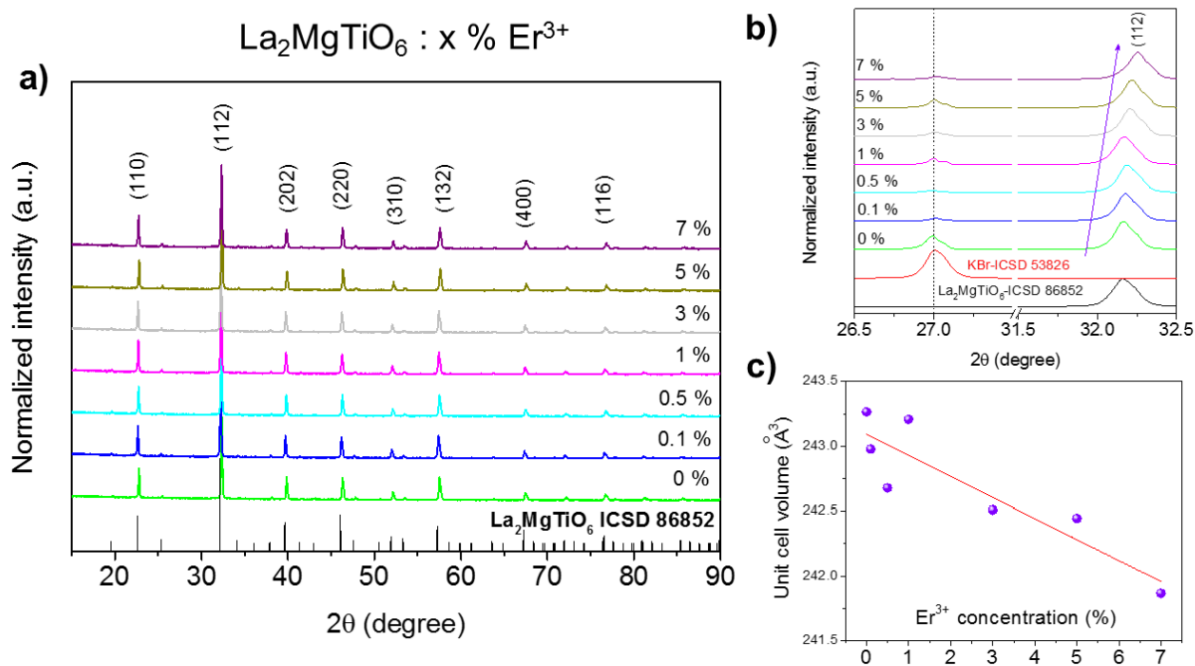


**Figure 1.** (**a**) X-ray powder diffraction of $La_2MgTiO_6$:x $Er^{3+}$, (x = 0%, 0.1%, 0.5%, 1%, 3%, 5%, or 7%); (**b**) position correction of main diffraction peak of $La_2MgTiO_6$ with the help of KBr; (**c**) changing of unit cell volume as a function of $Er^{3+}$ concentration (in the inset).

Due to the similarity of charge and ionic radius (121.6 pm for $La^{3+}$ and 106.2 pm for $Er^{3+}$ with the same coordination number, CN = 9 [30]), it can be assumed that $Er^{3+}$ ions most likely substituted for $La^{3+}$ ions located in the $C_s$ symmetry site. Therefore, the replacement of smaller $Er^{3+}$ ions with larger $La^{3+}$ ions resulted in the contraction of the crystal structure at higher dopant concentration. In order to prove our hypothesis, the XRD of all samples was measured again with a pure powder of potassium bromide (KBr,

ICSD no. 53826), and the position of diffraction lines ($2\theta = 32.3°$) of $La_2MgTiO_6$ was corrected (Figure 1b). The observed right-shifting of the diffraction peaks (Figure 1b) and the shrinkage of the unit cell volume with an increase in $Er^{3+}$ concentration (Figure 1c) confirmed the above assumption. The concentration-dependent lattice parameters are shown in Figure S1 (Supplementary Materials).

The morphology and the energy-dispersive spectroscopy (EDS) X-ray microanalysis of LMT:5% $Er^{3+}$ are presented in Figures 2 and 3, respectively. From the SEM images, no individual grains were observed, and the grain size ranged from 0.5 to 1.0 mm, much smaller than that (5 μm) obtained via the conventional solid-state method [25]. It is clearly shown that small grains were strongly aggerated to form bigger objects. From the EDS measurements, all elemental compositions of LMT:5% $Er^{3+}$ were identified and quantified including La (59.32 wt.%), Er (3.97 wt.%), Mg (6.18 wt.%), Ti (11.8 wt.%), and O (18.73 wt.%). These values are consistent with the general chemical formula: La (58.8 wt.%), Er (3.73 wt.%), Mg (5.41 wt.%), Ti (10.67 wt.%), and O (21.39 wt.%).
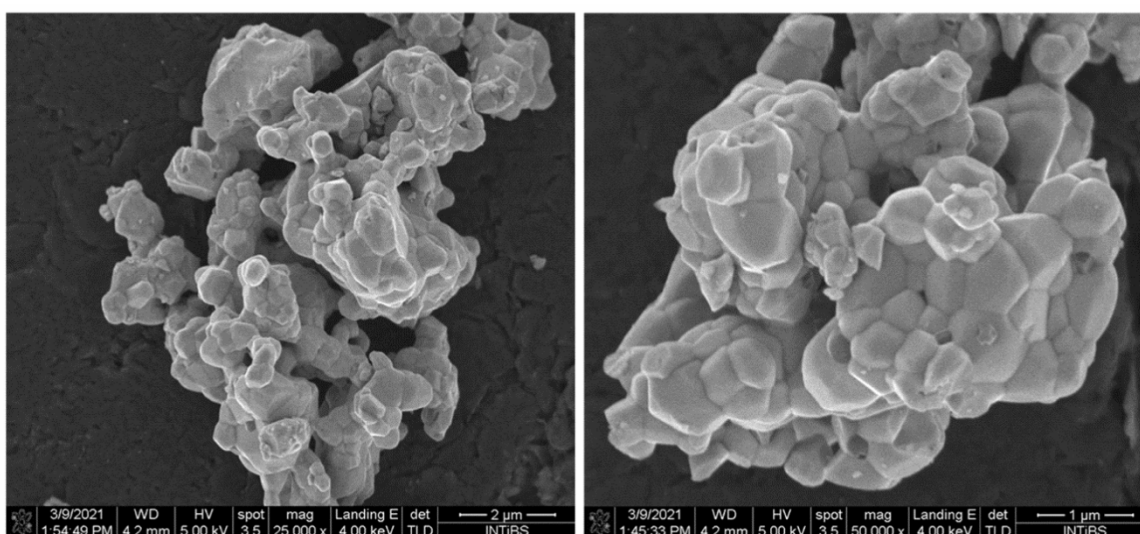


**Figure 2.** SEM images of sample $La_2MgTiO_6$:5% $Er^{3+}$.



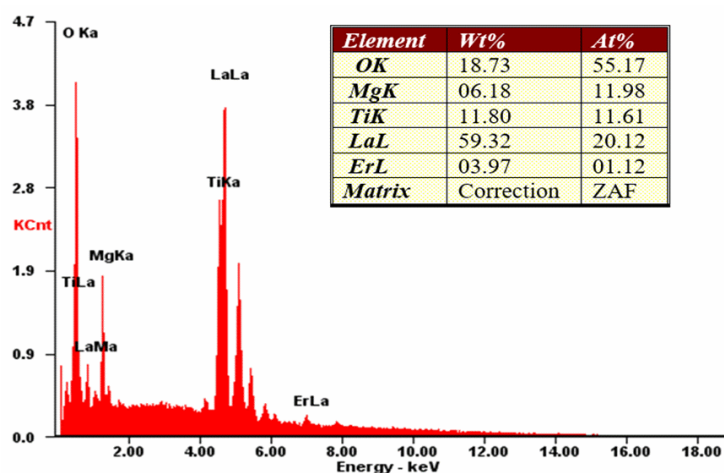| Element | Wt% | At% |
|---------|-----|-----|
| OK | 18.73 | 55.17 |
| MgK | 06.18 | 11.98 |
| TiK | 11.80 | 11.61 |
| LaL | 59.32 | 20.12 |
| ErL | 03.97 | 01.12 |
| Matrix | Correction | ZAF |

**Figure 3.** Results of EDS X-ray microanalysis of $La_2MgTiO_6$:5% $Er^{3+}$.

*3.2. Absorption Spectrum*

The absorption spectrum of LMT:7% $Er^{3+}$ in the range of 200–2000 nm, shown in Figure 4, exhibited typical transitions for $Er^{3+}$ ions. Intense absorption bands starting from 200 nm up to 350 nm were attributed to the absorption of the host. In accordance with previous studies [6,31–33], the obtained absorption lines were well assigned to the

typical f–f transitions of $Er^{3+}$ ions from ground state $^4I_{15/2}$ to the successive excited states including $^4G_{7/2}$, $^4G_{9/2}$, $^4G_{11/2}$, $^2H_{9/2}$, $^4F_{5/2}$, $^4F_{7/2}$, $^2H_{11/2}$, $^4S_{3/2}$, $^4F_{9/2}$, $^4I_{9/2}$, $^4I_{11/2}$, and $^4I_{13/2}$, among which, $^4I_{15/2} \rightarrow {}^4G_{11/2}$ was the dominant one (see the inset in Figure 4).
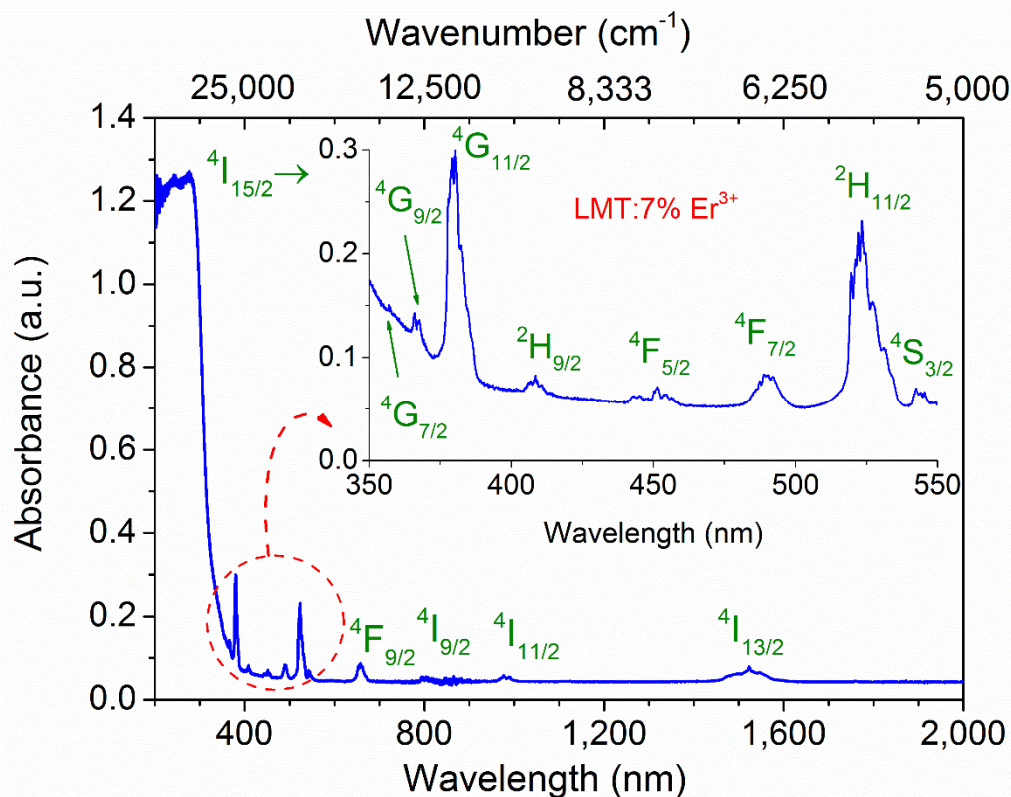


**Figure 4.** Absorption spectrum of $La_2MgTiO_6$:7% $Er^{3+}$ at room temperature.

To determine the energy of the forbidden bandgap of the host and the sample doped with 7% $Er^{3+}$, the modified Kubelka–Munk function (also known as the Tauc method) [34] was applied to the 300 K absorption spectra. The energy gap between the top of the valence band and the bottom of the conduction band of the host and LMT:7% $Er^{3+}$ were found to be 4.06 eV and 4.07 eV, respectively (Figure 5). The insignificant difference between them could have resulted from a measurement error. This value was slightly higher than that (3.98 eV) obtained for the same $Pr^{3+}$-doped host [17].
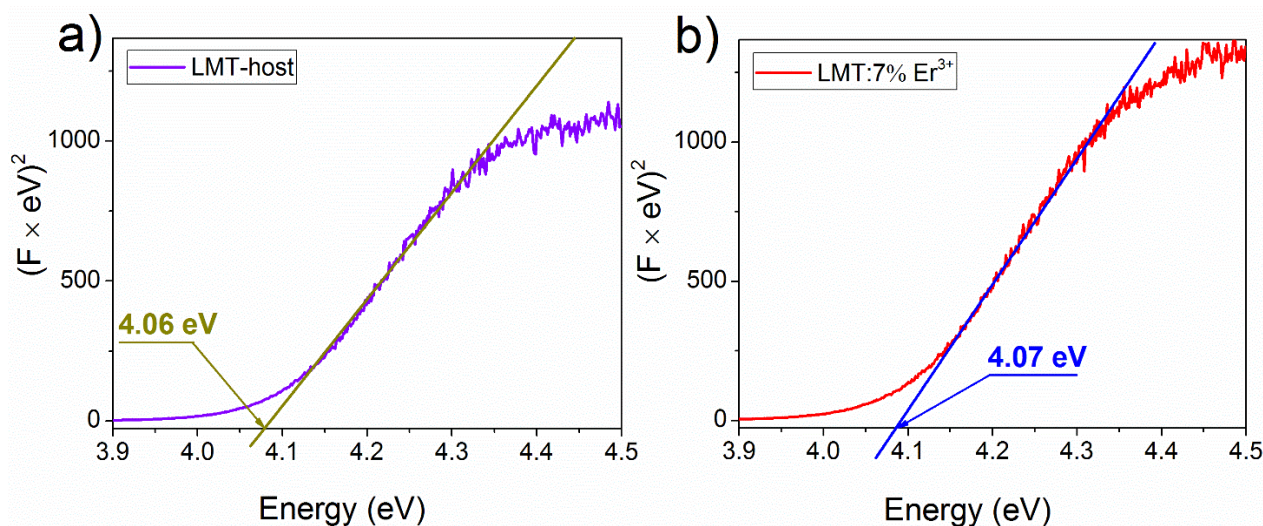


**Figure 5.** Forbidden energy bandgaps ($E_g$) of $La_2MgTiO_6$ host (**a**) and $La_2MgTiO_6$:7% $Er^{3+}$ (**b**) calculated from the absorption spectra obtained from the reflection spectra applying the modified Kubelka–Munk function (also known as the Tauc method).

### 3.3. Luminescence Studies

A wide spectral range from visible to the near-infrared of LMT doped with different concentrations of $Er^{3+}$ ions, observed for 266 nm wavelength direct excitation of $TiO_6$ groups, is shown in Figure 6. As can be seen, there was no difference in the shape of the emission spectrum across the samples. According to the absorption spectrum (Figure 4) and the emission spectra (Figure 6), the assignment of all energy levels of $Er^{3+}$ ions was tabulated in Table S1.
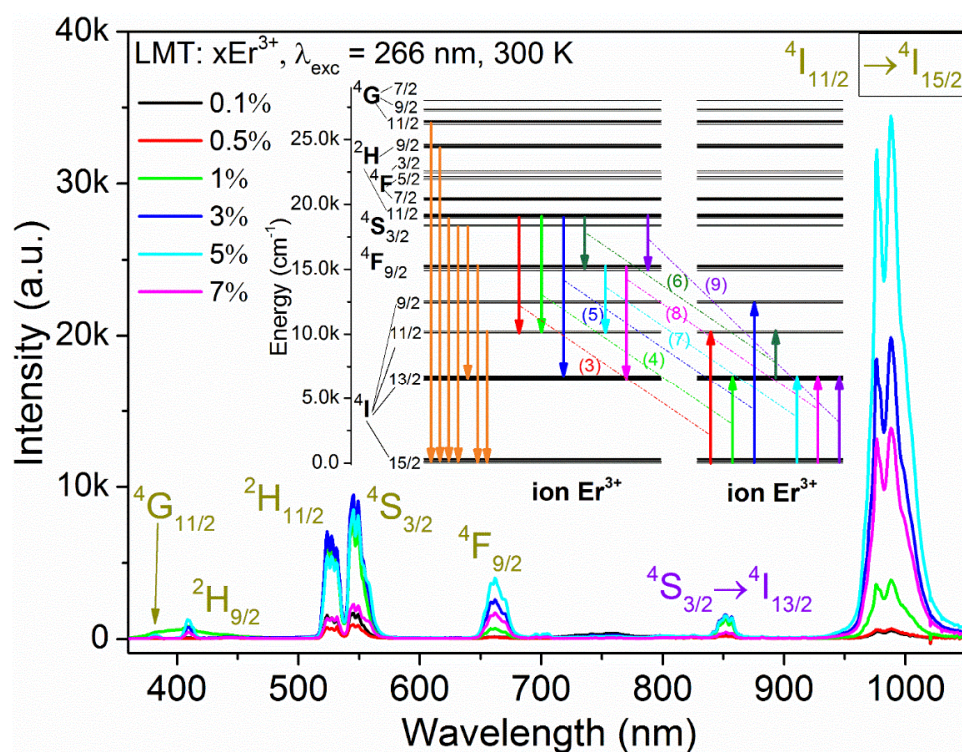


**Figure 6.** The 300 K emission spectra of $La_2MgTiO_6$:x $Er^{3+}$ (x = 0.1%, 0.5%, 1%, 3%, 5%, or 7%) recorded under a 266 nm excitation Nd:YAG line. Inset: Some possible cross-relaxation processes in $La_2MgTiO_6$:$Er^{3+}$.

Similarly to the LMT samples doped with $Eu^{3+}$ [3] and $Nd^{3+}$ [2], a broad emission band of $TiO_6$ groups also appeared from 400 nm to 550 nm at 77 K (Figure S2). The energy transfer from $TiO_6$ groups to $Er^{3+}$ ions was perfectly exemplified by temperature and $Er^{3+}$ concentration. A higher $Er^{3+}$ content resulted in a lower intensity of the emission of $TiO_6$ groups. This process was also facilitated by elevating temperature. No $TiO_6$ emission was observed at room temperature (Figure 6). For visible emission including $^2H_{11/2}$, $^4S_{3/2}$, and $^4F_{9/2}$ to the ground state, $^4I_{15/2}$ located in the green, yellow, and red regions was centered at 531.7 nm (18,807 $cm^{-1}$), 549 nm (18,215 $cm^{-1}$), and 662 nm (15,106 $cm^{-1}$), respectively. In addition, infrared emission from $^4I_{11/2}$ and $^4I_{13/2}$ levels to the ground state was maximum at 988 nm (10,121 $cm^{-1}$) and 1524 nm (6562 $cm^{-1}$), respectively (Figure S3). Furthermore, the emission spectra were also contributed to by a few less intense transitions corresponding to $^4G_{11/2}$, $^2H_{9/2} \rightarrow {}^4I_{15/2}$, and $^4S_{3/2} \rightarrow {}^4I_{13/2}$ levels.

The energy difference ($\Delta E$) between $^2H_{11/2}$ and $^4S_{3/2}$ was 592 $cm^{-1}$; this value is similar to that found in $LaAlO_3$:$Er^{3+}$ with 660 $cm^{-1}$ [6]. Due to the small energy difference, the transition from $^2H_{11/2}$ to ground state can be easily populated at room temperature by thermalization (see Figure 6).

Temperature plays an important role in the thermal population of $^2H_{11/2}$ from the $^4S_{3/2}$ level. It is regulated by the following Boltzmann distribution formula:

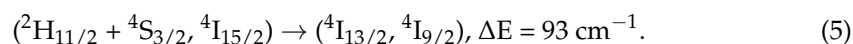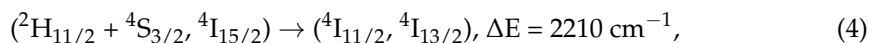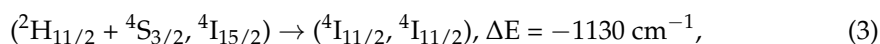$$\frac{N_A}{N_B} = \frac{g_A}{g_B} \exp\left(\frac{-\Delta E}{kT}\right), \tag{1}$$

where $N_A$ ($N_B$) is the population of level $^2H_{11/2}$ ($^4S_{3/2}$), $g_A$ ($g_B$) is the degeneration of level $^2H_{11/2}$ ($^4S_{3/2}$), k is the Boltzmann constant, and $\Delta E$ is the energy difference between these levels. These levels were further considered in terms of temperature sensing.

Moreover, the integrated emission intensity of all samples is plotted in the inset. It can be clearly seen that the integrated intensity moderately increased with $Er^{3+}$ concentration. The highest intensity was achieved for the sample doped with 5% $Er^{3+}$ (Figure S4). Above this threshold value, the intensity decreased as a result of concentration quenching. This phenomenon could result from an exchange interaction or multipolar interaction depending on the critical transfer distance $R_c$ between $Er^{3+}$ ions. Therefore, to better understand, Blasse's model was applied [35].

$$R_C = 2 \times \left(\frac{3V}{4\pi x_C N}\right)^{1/3}, \tag{2}$$

where V is the unit cell volume, and $x_c$ is the quenching concentration. For samples doped with 5% $Er^{3+}$, V = 242.45 $Å^3$, $x_c$ = 0.05, and N = 4. The value of $R_C$ was equal to 13.2 Å, indicating that the quenching mechanism which occurred in LMT:$Er^{3+}$ samples was predominantly regulated by the electric multipolar interaction. A similar phenomenon was previously observed in LMT doped with $Nd^{3+}$ ions [2].

The analysis of the emission spectra of LMT:$Er^{3+}$ allowed concluding that, with the increase in the concentration of doping ions, two competing phenomena are observed. The increased amount of $Er^{3+}$ ions initially led to an increase in the emission intensity of all bands (see Figure S5); however, the intensity of each of these bands changed differently depending on the $Er^{3+}$ concentration. Due to thermalization at 300 K, both $^2H_{11/2}$ and $^4S_{3/2}$ levels could be regarded as one. It can be seen that, in the range 1–5% $Er^{3+}$, the emission intensity of $^4S_{3/2}$ remained almost constant with a local maximum for 3%. On the other hand, the emission of the $^4F_{9/2}$ and $^4I_{11/2}$ levels increased from the 0.5% $Er^{3+}$ concentration. This was mainly to the detriment of the ($^2H_{11/2}$, $^4S_{3/2}$) level, which transferred energies to these lower levels in the process of cross-relaxation. As the dopant concentration increased, the likelihood of these processes increased as a function of the number of $Er^{3+}$ ion pairs. If one of the ions in a pair was excited and the other was not, the first would be the donor and the second would be the acceptor, and the energy transfer processes could be described as follows:

$$(^2H_{11/2} + {}^4S_{3/2}, {}^4I_{15/2}) \rightarrow ({}^4I_{11/2}, {}^4I_{11/2}), \Delta E = -1130 \text{ cm}^{-1}, \tag{3}$$

$$(^2H_{11/2} + {}^4S_{3/2}, {}^4I_{15/2}) \rightarrow ({}^4I_{11/2}, {}^4I_{13/2}), \Delta E = 2210 \text{ cm}^{-1}, \tag{4}$$

$$(^2H_{11/2} + {}^4S_{3/2}, {}^4I_{15/2}) \rightarrow ({}^4I_{13/2}, {}^4I_{9/2}), \Delta E = 93 \text{ cm}^{-1}. \tag{5}$$

At continuous wave excitation, the $^4I_{13/2}$ level would be populated; therefore, it is possible to write another path of the CR process as follows:

$$(^2H_{11/2} + {}^4S_{3/2}, {}^4I_{13/2}) \rightarrow ({}^4I_{9/2}, {}^4I_{11/2}), \Delta E = 436 \text{ cm}^{-1}. \tag{6}$$
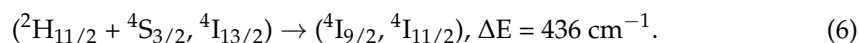
The $^4I_{11/2}$ level could also be fed in another cross-relaxation process from the $^4F_{9/2}$ level as follows:

$$(^4F_{9/2}, {}^4I_{15/2}) \rightarrow ({}^4I_{11/2}, {}^4I_{13/2}) \Delta E = -1530 \text{ cm}^{-1}. \tag{7}$$
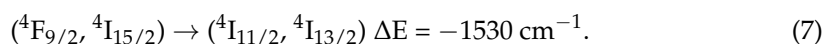
The $^4F_{9/2}$ level could also be drained by the following process:

$$(^4F_{9/2}, {}^4I_{15/2}) \rightarrow (^4I_{13/2}, {}^4I_{13/2}) \; \Delta E = 1500 \text{ cm}^{-1}. \tag{8}$$
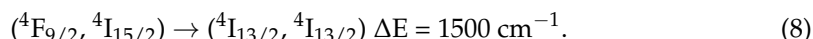
There was a certain probability of the following CR populating the $4F_{9/2}$ level:

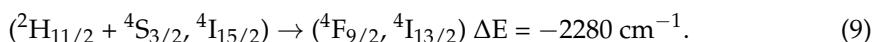$$(^2H_{11/2} + {}^4S_{3/2}, {}^4I_{15/2}) \rightarrow (^4F_{9/2}, {}^4I_{13/2}) \; \Delta E = -2280 \text{ cm}^{-1}. \tag{9}$$

Please note that the maximum energy phonon of this host was found to be 741 cm$^{-1}$ [36]. In the processes described by Equations (3), (7), and (9), there is a shortage of energy, which can easily be obtained from the crystal lattice at 300 K. These are phonon-assisted processes; however, the process described by Equation (9), requiring the assistance of up to three phonons, is the least likely in this list. In the processes described by Equations (4) and (8), a small excess of energy would be easily absorbed by the crystal lattice. All processes are pictured in the inset of Figure 6.

### 3.4. Luminescent Decay Profiles

To better understand the quenching behavior of the green, red, and IR emission, the decay profiles of some samples at room temperature, registered at 549 nm, 662 nm, and 988 nm corresponding to $^4S_{3/2}$, $^4F_{9/2}$, and $^4I_{11/2}$ levels were taken into account (Figure S6). Nonexponential decay was observed for the samples doped with more than 1% Er$^{3+}$. Due to the thermalization phenomenon, the decay of the $^4S_{3/2}$ level consisted of two components attributed to $^4S_{3/2}$ and $^2H_{11/2}$, respectively. Similarly, nonexponential luminescent decay monitored at $^4F_{9/2}$ was contributed by the $^4F_{9/2}$ and $^4S_{3/2}$ levels. The decay time of $^4F_{9/2}$ level was twofold shorter than that of the $^4S_{3/2}$ level observed for the samples containing less than 3% Er$^{3+}$. Among these levels, the decay time of the $^4I_{11/2}$ level was the longest one, as also observed for LaAlO$_3$:Er$^{3+}$ [6]. In addition, a very fast rise time was obtained for all samples as a result of cross-relaxation processes (Figure S6 and Table S2).

Figure S5 shows the integrated emission intensity of some levels, including $^2H_{11/2}$ ($I_2$), $^4S_{3/2}$ ($I_3$), $^4F_{9/2}$ ($I_4$), and $^4I_{11/2}$ ($I_6$) to ground state $^4I_{15/2}$. The observed emission of each level can be contributed by radiative emission or nonradiative relaxation (multi-phonon relaxation) and cross-relaxation phenomena.

As can be clearly seen, the 300 K decay profiles upon 266 nm excitation (except for the sample doped with 0.1% Er$^{3+}$) exhibited a nonexponential behavior on account of the energy transfer between Er$^{3+}$ ions (Figure 7). Thus, the Inokuti–Hirayama model was used to calculate the critical transfer distance $R_0$ and the critical concentration $C_0$ by the following equation [37]:

$$I_t = I_0 \exp^{\left[ \frac{-t}{\tau} - \alpha \times \left( \frac{t}{\tau} \right)^{\frac{3}{S}} \right]} + (\text{offset}), \tag{10}$$

where $I_0$, $I_t$ represent the emission intensity at t = 0 and after pulse excitation, $\tau$ is the radiative decay time, C is the Er$^{3+}$ concentration, $C_0$ is the Er$^{3+}$ critical concentration, $\Gamma\left(1 - \frac{3}{S}\right)$ is the gamma function, S defines the dipole–dipole, dipole–quadrupole, and quadrupole–quadrupole interactions corresponding to S = 6, 8, and 10, respectively, and Q is the energy transfer parameter [37–40].

$$\alpha = \frac{4\pi}{3} \times \Gamma\left(1 - \frac{3}{S}\right) \times C \times R_0^3, \tag{11}$$

where $R_0$ stands for the critical transfer distance at which the energy transfer efficiency achieves 50% and is equal the radiative decay rate $\tau_0^{-1}$.
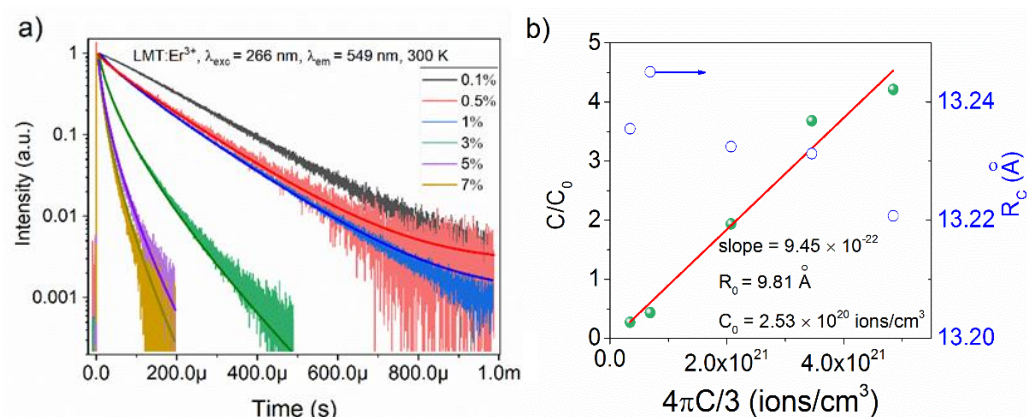
**Figure 7.** (**a**) The 300 K decay profiles under 266 nm excitation, monitored at 549 nm and fitted to the Inokuti–Hirayama function (solid lines) for S = 6; (**b**) critical transfer distance $R_0$ and critical concentration $C_0$ calculated from the slope of the plot of $(C/C_0)$ vs. $(4\pi C/3)$ and the interionic distance between dopants ($R_c$) of all $Er^{3+}$-doped samples (right $Y$-axis).

The correlation of C, $C_0$, $R_0$ can be derived from Equations (10) and (11) to yield the following formula [37–40]:

$$\frac{C}{C_0} = \frac{4\pi C R_0^3}{3}. \tag{12}$$

The donor–acceptor energy transfer parameter ($C_{da}$) and the energy transfer probability ($W_{da}$) can be calculated using the following equations [40–43]:

$$C_{da} = R_0^6 \times \tau_0^{-1}, \tag{13}$$

$$W_{da} = R_0^{-6} \times C_{da} = \tau_0^{-1}. \tag{14}$$

The energy transfer decay rates of the samples as a function of $Er^{3+}$ concentration can be estimated as follows:

$$W_{tot} = W_{rad} + W_{da} = \frac{1}{\tau_{rad}} + W_{da}, \tag{15}$$

where $\tau_{rad}$ is supposedly equal to the decay time of the sample doped with 0.1% $Er^{3+}$ ($\tau_{rad}$ = 166 µs, Table S2).

$$W_{tot} = aC^n + b, \tag{16}$$

where n indicates the strength of the multipole interaction between dopants; a weak interaction is exhibited by n = 1, while a strong one is exhibited by n = 2 [43].

As seen in Figure 7, the dipole–dipole interaction was responsible for the energy transfer in all samples, as exemplified by the best-fitting curves for S = 6. The experimental data can be described by Equation (12) as a linear function of the density of $Er^{3+}$ ions (Figure 7b). The value of $R_0$ was 9.81 Å, similar to the $R_c$ derived from the Blasse model. However, it is worth emphasizing that the values have different physical meaning [44]. Furthermore, $C_0 = 2.53 \times 10^{20}$ ions/$cm^{-3}$, whereas $C_{da}$ and $W_{da}$ were estimated by considering the radiative decay time value of the sample doped with 0.1% $Er^{3+}$ as $\tau_{rad}$ = 166 µs. Thereafter, $C_{da}$ and $W_{da}$ were found to be $5.38 \times 10^{-39}$ $cm^6 \cdot s^{-1}$ and 6020 $s^{-1}$, respectively. With n = 1.8 obtained from the fitting curve (Figure S7), one can conclude that a strong interaction among $Er^{3+}$ ions happened in LMT at 300 K.

### 3.5. Temperature-Sensing Ability

Furthermore, the temperature dependence of the emission intensity of LMT 5% $Er^{3+}$ is presented in Figure 8 for the 77–398 K range, and the temperature-dependent integrated emission intensity of some levels is also shown in the inset. It is shown that the most intense

emission came from $^4S_{3/2} \to {}^4I_{15/2}$ ($I_3$). In general, $I_3$ and some other levels, including $^2H_{9/2} \to {}^4I_{15/2}$ ($I_1$), $^4S_{3/2} \to {}^4I_{13/2}$ ($I_5$), and $^4F_{3/2} \to {}^4I_{15/2}$ ($I_4$), are strongly depopulated by elevating temperature, especially $I_3$ since it acts as an energy pump for the $^2H_{11/2}$ x2192; $^4I_{15/2}$ transition ($I_2$) via the thermalization process. The emission of $I_2$ reached its maximum at 248 K, before being quenched very quickly at a higher temperature. On the other hand, the $^4I_{11/2} \to {}^4I_{15/2}$ transition ($I_6$) was quite stable, remaining mostly unchanged until 248 K, at which point it then exhibited a significant decrease.
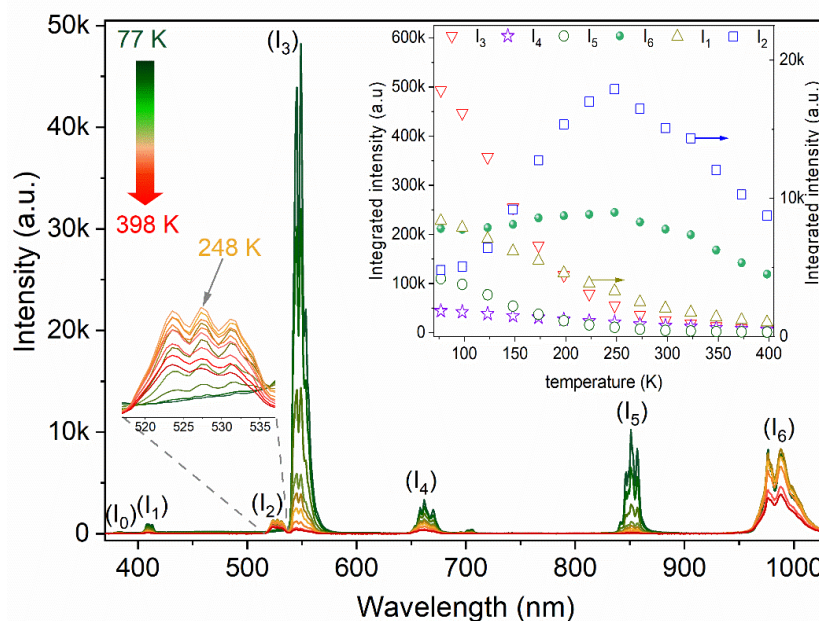


**Figure 8.** Temperature-dependent emission spectra of $La_2MgTiO_6$:5% $Er^{3+}$ excited at 266 nm in the range 77–398 K. Inset: Integrated emission intensity for distinct transitions as a function of temperature.

To verify the potential applicability of using LMT:$Er^{3+}$ as a noncontact thermometer, all possible combinations of $Er^{3+}$ emission bands were taken into account in the temperature range of 77–398 K (Figure 9). The first was devoted to the most frequently used, thermally coupled levels of $Er^{3+}$, including $^2H_{11/2} \to {}^4I_{15/2}$ and $^4S_{3/2} \to {}^4I_{15/2}$ (abbreviated as $I_2/I_3$) and a combination which also started from the same level $^4S_{3/2}$, i.e., $^2H_{11/2} \to {}^4I_{15/2}$ and $^4S_{3/2} \to {}^4I_{13/2}$ ($I_2/I_5$). The second was constructed on the basis of uncoupled levels; due to the different thermal behaviors through radiative emission, it is highly probable that these combinations would also be sensitive to temperature fluctuations.

The temperature-sensing performance of a thermometer can be evaluated through the absolute $S_a$ and relative sensitivity $S_r$ parameters. However, $S_a$ depends on the sample characteristics and experimental setup, whereas $S_r$ can be used for a comparison among distinct materials [24].

$$\Delta = \frac{I_i}{I_j}, \tag{17}$$

$$S_a = \frac{\partial \Delta}{\Delta T}, \tag{18}$$

$$S_r = \frac{1}{\Delta}\left|\frac{\partial \Delta}{\Delta T}\right|, \tag{19}$$

where thermometric parameter $\Delta$ is denoted as the ratio between two different emission levels $I_i$, $I_j$.
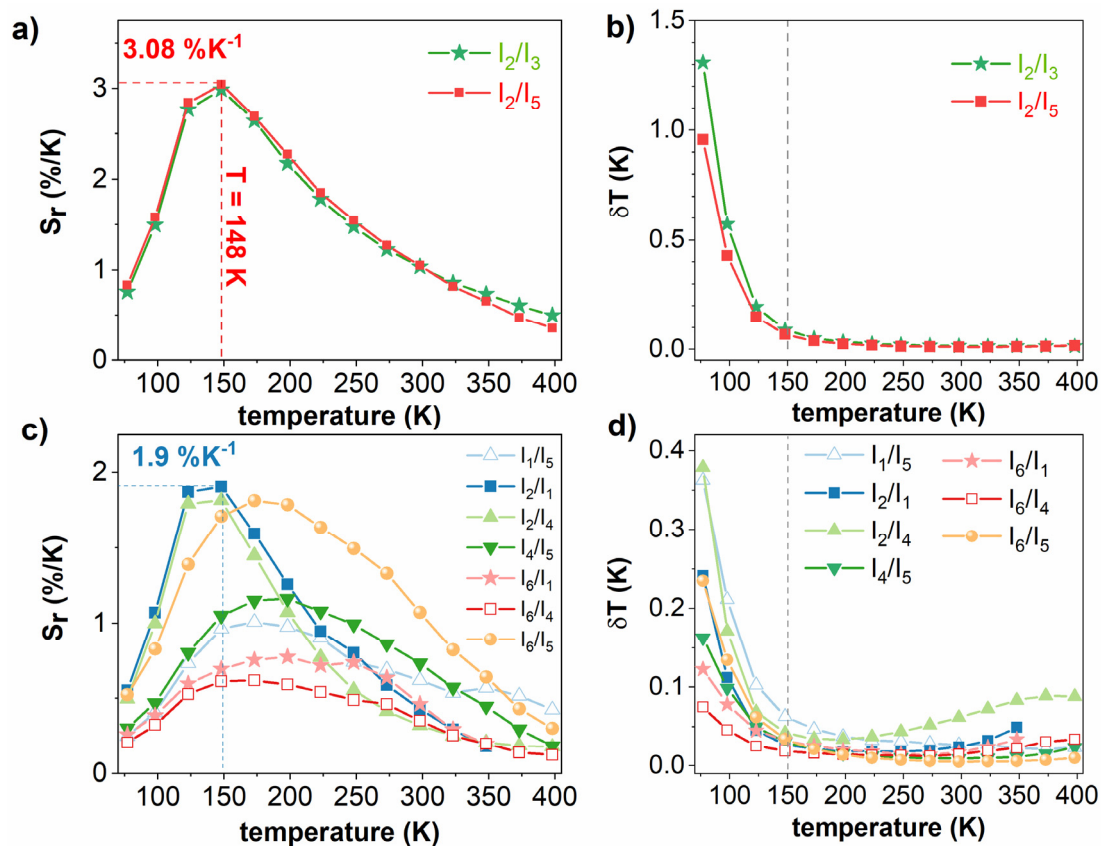
**Figure 9.** Relative sensitivities ($S_r$) and temperature uncertainties ($\delta T$) derived from thermometric parameters based on thermally coupled levels (**a**,**b**) and uncoupled levels (**c**,**d**).

For thermally coupled levels, the emission intensity of the $^2H_{11/2} \rightarrow {}^4I_{15/2}$ transition was strongly populated by thermalization via the $^4S_{3/2}$ level. As a result, the emission intensity of the transition coming from $^4S_{3/2}$ decreased, i.e., $^4S_{3/2} \rightarrow {}^4I_{15/2}$ ($I_3$) and $^4S_{3/2} \rightarrow {}^4I_{13/2}$ ($I_5$). However, $^4S_{3/2} \rightarrow {}^4I_{13/2}$ exhibited a steady quench with respect to $^4S_{3/2} \rightarrow {}^4I_{15/2}$, resulting in a much faster growth in the thermometric parameter and a higher absolute sensitivity ($S_a$) for $I_2/I_5$ (see Figure S8a,b). As shown in Figure 9, the relative sensitivities ($S_r$) of given coupled levels were identical as predicted, since both ($I_3$) and ($I_5$) originated from the same level $^4S_{3/2}$. The highest $S_r$ recorded at 148 K with the values of 2.98%·$K^{-1}$ and 3.08%·$K^{-1}$ corresponded to $I_2/I_3$ and $I_2/I_5$, respectively.

Regarding the thermally uncoupled levels, the $S_r$ values are plotted in Figure 9c. The best performance for temperature determination was obtained for the $I_2/I_1$ pair with 1.9%·$K^{-1}$ at 148 K.

It is crucial to note that higher relative sensitivity does not imply more reliable results. Therefore, temperature uncertainty ($\delta T$), which is usually intentionally ignored, was determined using the below equation [24].

$$\delta T = \frac{1}{S_r} \frac{\delta \Delta}{\Delta}. \tag{20}$$

$\delta T$ is known as the smallest change in temperature which can be detected by the measurement. In the range from 77–150 K, $\delta T$ was found to be less than 1.3 K and 0.4 K for coupled levels and uncoupled levels, respectively. From 150–400 K, the values were found to be less than 0.1 K in both cases (Figure 9b,d).

Table 1 presents the relative sensitivities of numerous materials doped or co-doped with $Er^{3+}$ ions. The results in this work completely dominate in comparison with other compounds investigated in the literature. For some samples studied on both thermally

coupled and uncoupled levels, it can be seen that the thermally coupled levels had higher sensitivity. However, only a few transitions can work as thermally coupled levels, while many uncoupled levels can provide more promising pairs across the different temperature ranges. Furthermore, the introduction of some co-dopants ($Y^{3+}$, $La^{3+}$, $Yb^{3+}$) into the $Er^{3+}$-doped system was not only to enhance the green up-conversion emission of $Er^{3+}$ ions, but also to create more potential pairs to tackle the limitations of the thermally coupled level-based optical thermometer.

**Table 1.** The maximum relative sensitivity $S_m$ (%·$K^{-1}$) of some materials doped with $Er^{3+}$ corresponding to thermally coupled level and uncoupled levels at temperature $T_m$ (K) with temperature uncertainty $\delta T_m$ (K).

| Material | $\lambda_{exc}$ (nm) | Temperature Range (K) | $S_m$ (%·$K^{-1}$) | $T_m$ (K) | $\delta T_m$ (K) | References |
|---|---|---|---|---|---|---|
| $Al_2O_3$:$Er^{3+}$, $Y^{3+}$ | 978 | 295–973 | 0.35 | 450 | 0.3 | [45] |
| $Sr_2CaWO_6$:$Er^{3+}$, $La^{3+}$ | 980 | 250–2000 | 0.5 | 439 | - | [46] |
| $NaNbO_3$:$Er^{3+}$ | 976 | 293–353 | 0.51 | 355 | - | [47] |
| $NaLaMgWO_6$:$Er^{3+}$ | 378 | 303–483 | 1.04 | 303 | - | [48] |
| $Gd_2O_3$:$Er^{3+}$, $Yb^{3+}$ | 980 | 300–550 | 1.18 | 300 | - | [49] |
| $Y_2O_3$:$Er^{3+}$ Coupled levels | 379 | 296–500 | 1.54 | 483 | - | [18] |
| Uncoupled levels | 379 | 303–434 | 0.87 | 434 | - | [18] |
| $LiLaMgWO_6$:$Er^{3+}$ | 378 | 303–483 | 2.24 | 483 | - | [29] |
| $Y_3Ga_5O_{12}$:$Er^{3+}$ | 488 | 300-850 | 0.64 | 547 | - | [50] |
| $La_2MgTiO_6$:$Er^{3+}$ (solid-state) | 380 | 303–483 | 1.107 | 303 | - | [25] |
| $La_2MgTiO_6$:$Er^{3+}$ (coprecipitation) Coupled levels | 266 | 77–398 | 2.98 | 148 | 0.09 | This work |
| Uncoupled levels | 266 | 77–398 | 1.9 | 148 | 0.027 | This work |

The obtained result is also easily comparable with various dopants, such as LMT: $Pr^{3+}$ $S_r$ = 1.28%·$K^{-1}$ at 350 K [17], LMT:$Eu^{3+}$ $S_r$ = 3%·$K^{-1}$ at 77 K [3], LMT:$Nd^{3+}$ $S_r$ = 0.83%·$K^{-1}$ at 275 K [2], and LMT:$V^{5+}$ and $Cr^{3+}$ $S_r$ = 1.96%·$K^{-1}$ at 165 K [1]. Such an exceptional value of $S_r$ of 2.98%·$K^{-1}$ at 148 K demonstrates LMT:5% $Er^{3+}$ as a potential candidate for temperature readout at low temperature.

## 4. Conclusions

In this study, $La_2MgTiO_6$:$Er^{3+}$ was prepared via the coprecipitation method. All samples crystallized in n orthorhombic structure with the space group *Pbnm* (62). The chemical composition of the representative sample was in agreement with the theoretical chemical composition. The morphology of the sample was inhomogeneous, and the grain size was distributed in the micro range, from 0.5 to 1 μm. The energy transfer among $Er^{3+}$ ions occurred predominantly via dipole–dipole interactions. The critical transfer distance $R_0$, critical concentration $C_0$, energy transfer parameter $C_{da}$, and energy transfer probability $W_{da}$ were found to be 9.81 Å, 2.53 × $10^{20}$ ions·$cm^{-3}$, 5.38 × $10^{-39}$ $cm^6$·$s^{-1}$, and 6020 $s^{-1}$, respectively. More importantly, the low-temperature-sensing ability of $La_2MgTiO_6$:5% $Er^{3+}$ was explored using the ratio of emission intensity of the thermally coupled and uncoupled energy levels. The thermally coupled energy levels $^2H_{11/2} \rightarrow {}^4I_{15/2}$ and $^4S_{3/2} \rightarrow {}^4I_{15/2}$ exhibited the greatest sensitivity of around 2.98%·$K^{-1}$ at 148 K, and the uncertainty was less than 1 K in the range of 77–398 K. The abovementioned findings indicate the huge potential of $La_2MgTiO_6$:$Er^{3+}$ for temperature-sensing operating at low temperature.

rise time (in the inset) excited at 266 nm and monitored at 549 nm (a), at 662 nm (b), at 988 nm (c). Figure S7: Energy transfer rates Wtot = aCn at 300 K as a function of $Er^{3+}$ concentration. Figure S8. Thermometric parameters (a) and absolute sensitivities, Sa (K-1) (b) based on thermally coupled levels; Thermometric parameters (c) and absolute sensitivities, Sa (K-1) (d) based on thermally uncoupled levels. Table S1: Energy levels of $Er^{3+}$ ions in $La_2MgTiO_6$ double perovskites obtained from the 77 K and 300 K emission spectra and the 300 K absorption spectrum *. Table S2: Decay time of $La_2MgTiO_6$:$Er^{3+}$ obtained at different monitoring wavelength corresponding to 4S3/2 (549 nm), $4F_{9/2}$ (662 nm), $4I_{11/2}$ (988 nm) levels and their rise time (*) single-exponential decay for the sample $La_2MgTiO_6$:0.1% $Er^{3+}$.

**Author Contributions:** Conceptualization, T.H.Q.V.; data curation, T.H.Q.V. and B.B.; formal analysis, T.H.Q.V., B.B., D.S. and P.J.D.; funding acquisition, P.J.D.; investigation, T.H.Q.V., B.B., D.S. and P.J.D.; methodology, T.H.Q.V., B.B. and D.S.; project administration, P.J.D.; resources, T.H.Q.V. and B.B.; supervision, D.S. and P.J.D.; validation, T.H.Q.V., B.B. and P.J.D.; visualization, T.H.Q.V.; writing— original draft, T.H.Q.V.; writing—review and editing, T.H.Q.V., B.B., D.S. and P.J.D. All authors have read and agreed to the published version of the manuscript.

**Institutional Review Board Statement:** Not applicable.

**Informed Consent Statement:** Not applicable.

**Data Availability Statement:** Data is contained within the article or supplementary material.

**Conflicts of Interest:** The authors declare no conflict of interest.

## References

1. Stefańska, D.; Bondzior, B.; Vu, T.H.Q.; Grodzicki, M.; Dereń, P.J. Temperature sensitivity modulation through changing the vanadium concentration in a $La_2MgTiO_6$:$V^{5+}$,$Cr^{3+}$ double perovskite optical thermometer. *Dalton Trans.* **2021**, *50*, 9851–9857. [CrossRef]
2. Vu, T.; Bondzior, B.; Stefańska, D.; Dereń, P. Influence of temperature on near-infrared luminescence, energy transfer mechanism and the temperature sensing ability of $La_2MgTiO_6$:$Nd^{3+}$ double perovskites. *Sensors Actuators A Phys.* **2021**, *317*, 112453. [CrossRef]
3. Bondzior, B.; Stefańska, D.; Vũ, T.; Miniajluk-Gaweł, N.; Dereń, P. Red luminescence with controlled rise time in $La_2MgTiO_6$:$Eu^{3+}$. *J. Alloys Compd.* **2021**, *852*, 157074. [CrossRef]
4. Antic-Fidancev, E.; Deren, P.; Krupa, J.-C. Energy levels and crystal field calculations of $Er^{3+}$ in $LaAlO_3$. *J. Alloys Compd.* **2004**, *380*, 376–379. [CrossRef]
5. Dereń, P.; Mahiou, R.; Pazik, R.; Lemanski, K.; Strek, W.; Boutinaud, P. Upconversion emission in $CaTiO_3$:$Er^{3+}$ nanocrystals. *J. Lumin.* **2008**, *128*, 797–799. [CrossRef]
6. Deren, P.; Mahiou, R. Spectroscopic characterisation of $LaAlO_3$ crystal doped with $Er^{3+}$ ions. *Opt. Mater.* **2007**, *29*, 766–772. [CrossRef]
7. Su, B.; Xie, H.; Tan, Y.; Zhao, Y.; Yang, Q.; Zhang, S. Luminescent properties, energy transfer, and thermal stability of double perovskites $La_2MgTiO_6$:$Sm^{3+}$, $Eu^{3+}$. *J. Lumin.* **2018**, *204*, 457–463. [CrossRef]
8. Li, W.; Chen, T.; Xia, W.; Yang, X.; Xiao, S. Near-infrared emission of $Yb^{3+}$ sensitized by $Mn^{4+}$ in $La_2MgTiO_6$. *J. Lumin.* **2018**, *194*, 547–550. [CrossRef]
9. Srivastava, A.; Comanzo, H.; Brik, M. Luminescence of $Bi_{3+}$ in the double perovskite, $La_2MgTiO_6$. *Opt. Mater.* **2018**, *75*, 809–813. [CrossRef]
10. Yin, X.; Yao, J.; Wang, Y.; Zhao, C.; Huang, F. Novel red phosphor of double perovskite compound $La_2MgTiO_6$:x $Eu^{3+}$. *J. Lumin.* **2012**, *132*, 1701–1704. [CrossRef]
11. Huang, J.; Qin, M.; Yu, J.; Ma, A.; Yu, X.; Liu, J.; Zheng, Z.; Wang, X. $La_2MgTiO_6$:$Eu^{2+}$/$TiO_2$-based composite for methyl orange (MO) decomposition. *Appl. Phys. A* **2019**, *125*, 862. [CrossRef]
12. Srivastava, A.M.; Brik, M.G.; Comanzo, H.A.; Beers, W.W.; Cohen, W.E.; Pocock, T. Spectroscopy of $Mn^{4+}$ in Double Perovskites, $La_2LiSbO_6$ and $La_2LiSbO_6$: Deep Red Photon Generators for Agriculture LEDs. *ECS J. Solid State Sci. Technol.* **2018**, *7*, R3158–R3162. [CrossRef]
13. Li, L.; Qin, F.; Zhou, Y.; Miao, J.; Zhang, Z. Origin of the giant thermal enhancement of the $Er^{3+}$ ion's $4I_{9/2}$-$4I_{15/2}$ photoluminescence. *Spectrochim. Acta Part A Mol. Biomol. Spectrosc.* **2020**, *229*, 117862. [CrossRef]

14. Gai, S.; Zhu, H.; Gao, P.; Zhou, C.; Kong, Z.; Molokeev, M.S.; Qi, Z.; Zhou, Z.; Xia, M. Structure analysis, tuning photoluminescence and enhancing thermal stability on $Mn^{4+}$-doped $La_2$-xYxMgTiO_6 red phosphor for agricultural lighting. *Ceram. Int.* **2020**, *46*, 20173–20182. [CrossRef]

15. Takeda, Y.; Kato, H.; Kobayashi, M.; Kobayashi, H.; Kakihana, M. Photoluminescence Properties of $Mn^{4+}$-activated Perovskite-type Titanates, $La_2MTiO_6$:$Mn^{4+}$(M = Mg and Zn). *Chem. Lett.* **2015**, *44*, 1541–1543. [CrossRef]

16. Xie, H.; Su, B.; Tan, Y.; Zhao, Y.; Chai, S. Effect of $Gd^{3+}$, $Bi^{3+}$, or $Sm^{3+}$ on luminescent properties of $La_2-x\ MgTiO_6$:x $Eu^{3+}$ phosphors. *Luminescence* **2018**, *33*, 1450–1455. [CrossRef]

17. Shi, R.; Lin, L.-T.; Dorenbos, P.; Liang, H. Development of a potential optical thermometric material through photoluminescence of $Pr^{3+}$ in $La_2MgTiO_6$. *J. Mater. Chem. C* **2017**, *5*, 10737–10745. [CrossRef]

18. Brandão-Silva, A.C.; Gomes, M.A.; Novais, S.M.V.; Macedo, Z.S.; Avila, J.F.M.; Rodrigues, J.J.; Alencar, M.A.R.C. Size influence on temperature sensing of erbium-doped yttrium oxide nanocrystals exploiting thermally coupled and uncoupled levels' pairs. *J. Alloys Compd.* **2018**, *731*, 478–488. [CrossRef]

19. Rijckaert, H.; Kaczmarek, A.M. $Ho^{3+}$–$Yb^{3+}$ doped $NaGdF_4$ nanothermometers emitting in BW-I and BW-II. Insight into the particle growth intermediate steps. *Chem. Commun.* **2020**, *56*, 14365–14368. [CrossRef]

20. Stefańska, D.; Dereń, P.J. High Efficiency Emission of $Eu^{2+}$ Located in Channel and Mg-Site of $Mg_2Al_4Si_5O_{18}$ Cordierite and Its Potential as a Bi-Functional Phosphor toward Optical Thermometer and White LED Application. *Adv. Opt. Mater.* **2020**, *8*, 1–10. [CrossRef]

21. Stefańska, D.; Stefanski, M.; Dereń, P.J. Unusual emission generated from $Ca_2Mg_{0.5}AlSi_{1.5}O_7$:$Eu^{2+}$ and its potential for UV-LEDs and non-contact optical thermometry. *J. Alloys Compd.* **2021**, *863*, 158770. [CrossRef]

22. Trojan-Piegza, J.; Brites, C.D.S.; Ramalho, J.F.C.B.; Wang, Z.; Zhou, G.; Wang, S.; Carlos, L.D.; Zych, E. $La_{0.4}Gd_{1.6}Zr_2O_7$:0.1%Pr transparent sintered ceramic—A wide-range luminescence thermometer. *J. Mater. Chem. C* **2020**, *8*, 7005–7011. [CrossRef]

23. Sójka, M.; Brites, C.D.S.; Carlos, L.D.; Zych, E. Exploiting bandgap engineering to finely control dual-mode $Lu_2(Ge,Si)O_5$:$Pr^{3+}$ luminescence thermometers. *J. Mater. Chem. C* **2020**, *8*, 10086–10097. [CrossRef]

24. Brites, C.; Millán, A.; Carlos, L. Lanthanides in Luminescent Thermometry. *Metals* **2016**, 339–427. [CrossRef]

25. Hua, Y.; Yu, J.S. Strong Green Emission of Erbium(III)-Activated $La_2MgTiO_6$ Phosphors for Solid-State Lighting and Optical Temperature Sensors. *ACS Sustain. Chem. Eng.* **2021**, *9*, 5105–5115. [CrossRef]

26. Wade, S.; Collins, S.F.; Baxter, G. Fluorescence intensity ratio technique for optical fiber point temperature sensing. *J. Appl. Phys.* **2003**, *94*, 4743–4756. [CrossRef]

27. Ćirić, A.; Aleksić, J.; Barudžija, T.; Antić, Ž.; Đorđević, V.; Medić, M.; Periša, J.B.; Zeković, I.; Mitrić, M.; Dramićanin, M.D. Comparison of Three Ratiometric Temperature Readings from the $Er^{3+}$ Upconversion Emission. *Nanomaterials* **2020**, *10*, 627. [CrossRef]

28. Rakov, N.; Maciel, G.S. Exploring the $^4I_{13/2} \rightarrow {}^4I_{15/2}$ radiative transition from $Er^{3+}$ in $Y_2O_3$ for temperature sensing. *J. Lumin.* **2018**, *199*, 293–297. [CrossRef]

29. Ran, W.; Noh, H.M.; Park, S.H.; Lee, B.R.; Kim, J.H.; Jeong, J.H.; Shi, J.; Liu, G. Simultaneous bifunctional application of solid-state lighting and ratiometric optical thermometer based on double perovskite $LiLaMgWO_6$:$Er^{3+}$ thermochromic phosphors. *RSC Adv.* **2019**, *9*, 7189–7195. [CrossRef]

30. Shannon, R.D. Revised effective ionic radii and systematic studies of interatomic distances in halides and chalcogenides. *Acta Crystallogr. A* **1976**, *32*, 751–767. [CrossRef]

31. Ölsä, J.; Säilynoja, E.; Lamminmäki, R.-J.; Deren, P.; Strek, W.; Porcher, P. Crystal field energy level scheme of $Er^{3+}$ in GdOCl Parametric analysis. *J. Chem. Soc. Faraday Trans.* **1997**, *93*, 2241–2246. [CrossRef]

32. Stręk, W.; Dereń, P.; Maruszewski, K.; Pawlik, E.; Wojcik, W.; Malashkevich, G.; Gaishun, V.; Stręk, W. Spectroscopic properties of erbium doped silica glasses obtained by sol-gel method. *J. Alloys Compd.* **1998**, *275-277*, 420–423. [CrossRef]

33. Macalik, L.; Dereń, P.; Hanuza, J.; Stręk, W.; Demidovich, A.; Kuzmin, A. Effect of random distribution and molecular interactions on optical properties of $Er^{3+}$ dopant in $KY(WO_4)_2$ and $Ho^{3+}$ in $KYb(WO_4)_2$. *J. Mol. Struct.* **1998**, *450*, 179–192. [CrossRef]

34. López, R.; Gómez, R. Band-gap energy estimation from diffuse reflectance measurements on sol–gel and commercial $TiO_2$: A comparative study. *J. Sol-Gel Sci. Technol.* **2012**, *61*, 1–7. [CrossRef]

35. Blasse, G. Energy transfer in oxidic phosphors. *Phys. Lett. A* **1968**, *28*, 444–445. [CrossRef]

36. Levin, I.; Vanderah, T.A.; Amos, T.G.; Maslar, J.E. Structural Behavior and Raman Spectra of Perovskite-Like Solid Solutions (1 − x)$LaMg_{0.5}Ti_{0.5}O_{3-x}La_{2/3}TiO_3$. *Chem. Mater.* **2005**, *17*, 3273–3280. [CrossRef]

37. Inokuti, M.; Hirayama, F. Influence of Energy Transfer by the Exchange Mechanism on Donor Luminescence. *J. Chem. Phys.* **1965**, *43*, 1978–1989. [CrossRef]

38. Puchalska, M.; Watras, A. A clear effect of charge compensation through $Na^+$ co-doping on luminescent properties of new $CaGa_4O_7$:$Nd^{3+}$. *J. Alloys Compd.* **2016**, *688*, 253–260. [CrossRef]

39. Puchalska, M.; Watras, A. A clear effect of charge compensation through $Na^+$ co-doping on the luminescence spectra and decay kinetics of $Nd^{3+}$-doped $CaAl_4O_7$. *J. Solid State Chem.* **2016**, *238*, 259–266. [CrossRef]

40. Rudnicka, D.; Dereń, P. Preliminary spectroscopic properties of $K_4SrSi_3O_9$ doped with $Eu^{3+}$. *Opt. Mater.* **2013**, *35*, 2531–2534. [CrossRef]

41. Zheng, Y.; Chen, B.; Zhong, H.; Sun, J.; Cheng, L.; Li, X.; Zhang, J.; Tian, Y.; Lu, W.; Wan, J.; et al. Optical Transition, Excitation State Absorption, and Energy Transfer Study of $Er^{3+}$, $Nd^{3+}$ Single-Doped, and $Er^{3+}$/$Nd^{3+}$ Codoped Tellurite Glasses for Mid-Infrared Laser Applications. *J. Am. Ceram. Soc.* **2011**, *94*, 1766–1772. [CrossRef]

42. Llanos, J.; Espinoza, D.; Castillo, R. Energy transfer in single phase $Eu^{3+}$-doped $Y_2WO_6$ phosphors. *RSC Adv.* **2017**, *7*, 14974–14980. [CrossRef]

43. Bondzior, B.; Stefanska, D.; Kubiak, A.; Dereń, P. Spectroscopic properties of $K_4SrSi_3O_9$ doped with $Sm^{3+}$. *J. Lumin.* **2015**, *173*, 38–43. [CrossRef]

44. Bin Im, W.; Fellows, N.N.; Denbaars, S.; Seshadri, R.; Kim, Y.-I. $LaSr_2AlO_5$, a Versatile Host Compound for $Ce^{3+}$-Based Yellow Phosphors: Structural Tuning of Optical Properties and Use in Solid-State White Lighting. *Chem. Mater.* **2009**, *21*, 2957–2966. [CrossRef]

45. Dong, B.; Wang, X.J.; Li, C.R.; Liu, D.P. $Er^{3+}$-$Y^{3+}$-Codoped $Al_2O_3$ for High-Temperature Sensing. *IEEE Photon-Technol. Lett.* **2008**, *20*, 117–119. [CrossRef]

46. Wang, Y.; Liu, Y.; Shen, J.; Wang, X.; Yan, X. Controlling optical temperature behaviors of $Er^{3+}$ doped $Sr_2CaWO_6$ through doping and changing excitation powers. *Opt. Mater. Express* **2018**, *8*, 1926–1939. [CrossRef]

47. Kumar, K.U.; Santos, W.Q.; Silva, W.F.; Jacinto, C. Two photon thermal sensing in $Er^{3+}$/$Yb^{3+}$ Co-doped nanocrystalline $NaNbO_3$. *J. Nanosci. Nanotechnol.* **2013**, *13*, 6841–6845. [CrossRef] [PubMed]

48. Ran, W.; Noh, H.M.; Park, S.H.; Lee, B.R.; Kim, J.H.; Jeong, J.H.; Shi, J. $Er^{3+}$-Activated $NaLaMgWO_6$ double perovskite phosphors and their bifunctional application in solid-state lighting and non-contact optical thermometry. *Dalton Trans.* **2019**, *48*, 4405–4412. [CrossRef]

49. Šević, D.; Rabasovic, M.; Križan, J.; Savić-Šević, S.; Marinkovic, B.P.; Nikolic, M. Effects of temperature on luminescent properties of $Gd_2O_3$:Er, Yb nanophosphor. *Opt. Quantum Electron.* **2020**, *52*, 1–9. [CrossRef]

50. León-Luis, S.F.; Monteseguro, V.; Rodriguez-Mendoza, U.; Rathaiah, M.; Venkatramu, V.; Lozano-Gorrin, A.; Valiente, R.; Munoz, A.; Lavin, V. Optical nanothermometer based on the calibration of the Stokes and upconverted green emissions of $Er^{3+}$ ions in $Y_3Ga_5O_{12}$ nano-garnets. *RSC Adv.* **2014**, *4*, 57691–57701. [CrossRef]